physica status solidi a
www.pss-a.com

Check for updates

Nanopatterned SiN_x Broadband Antireflection Coating for Planar Silicon Solar Cells

Andrea Cordaro, Stefan Wil Tabernig,* Michael Pollard, Chuqi Yi, Esther Alarcon-Llado, Bram Hoex, and Albert Polman**

Crystalline Si solar cells based on thin wafers, with thicknesses in the range of 5–50 μm, can find applications in a wide range of markets where flexibility and bendability are important. For these cells, avoiding standard macroscopic texture is desirable to increase structural integrity. Herein, a nanopatterned SiN_x antireflection (AR) coating that consists of 174 nm-radius and 118 nm-high SiN_x nanodisks arranged in a square lattice on a thin (59 nm) SiN_x layer is introduced. This geometry combines Fabry–Pérot AR and forward scattering by a resonant Mie mode to achieve high transmission into the Si absorber over a broad spectral band. The nanostructured coating is patterned on a commercial interdigitated-back-contact (IBC) Si solar cell, experimentally demonstrating a short-circuit current density (J_{sc}) of 36.9 mA cm^{-2}, 2.3 mA cm^{-2} higher than for a single-layer AR coated cell, and an efficiency of 16.3% at a thickness of around 100 μm. It is shown that light incoupling efficiency is comparable to that of pyramidal texturing, while the absorption in the infrared is lower, due to less-effective light trapping. Overall, nanopatterned SiN_x broadband AR coatings are an appealing option for improving light management in ultrathin solar cells and other optoelectronic devices.

1. Introduction

Thin-film photovoltaics (PV) is becoming increasingly important for several reasons. First, thin-film absorbers require less material for fabrication, limiting costs, and promoting sustainable materials use. Second, thin-film PV can be flexible and bendable, which is important for the integration of aesthetically pleasing PV in buildings (BIPV[1,2]), curved PV on vehicles (VIPV[1,3–5]), integration with textiles,[6] and more. Flexible and durable solar cells can also be shaped and diced into arbitrary shapes, allowing for mass customization.[1]

The perspective of using thin, monocrystalline wafers of Si, the commercially most mature absorber material, for thin-film PV is an appealing prospect. Silicon is easy to bend and cut to a desired shape at thicknesses below 50 μm,[7,8] which is well below the common thickness of Si solar cells[9] (140–170 μm). From an electronic point of view, a thinner cell can have a larger open-circuit voltage (V_{oc})[10] due to reduced bulk recombination. However, to ensure optimum light absorption, the Si absorber needs to be thicker than 100 μm, as Si is a poor light absorber due to its indirect bandgap.[11]

Micrometer-sized random pyramidal texturing is the industry standard[12] for creating effective light incoupling and path length enhancement in wafer-based Si solar cells and is typically performed by etching in a KOH solution.[13] However, for very thin Si (<5 μm) wafers, the volume of standard texture would be a significant portion of the entire Si cell volume, compromising the mechanical integrity.

Several alternative geometries that do not exhibit large surface features and provide good incoupling and/or strong scattering have been developed recently. New chemical etch procedures have been developed to reduce the size of random pyramidal texturing, resulting in submicrometer features.[14–16] In such structures, careful surface passivation strategies resulted in performance comparable to standard micrometer-sized pyramids. Even though the open-circuit voltage (V_{oc}) still suffers from such an exposed area increase, this seems a promising route for thin-film PV. When features become even smaller (i.e., "black silicon" type of coatings[17,18]), surface passivation is a more severe challenge.

Recent work has investigated nanopatterned[19] and multilayer AR coatings[20] to effectively couple light into the solar cell and, in some cases, preferentially redirect light into angular channels at which light is trapped by total internal reflection within the absorber.[21–25]

Here, we introduce a single-layer periodic nanopattern of SiN_x disks combined with a planar SiN_x layer on the planar front

A. Cordaro, S. W. Tabernig, E. Alarcon-Llado, A. Polman
Center for Nanophotonics
NWO-Institute AMOLF
Science Park 104, 1098 XG Amsterdam, The Netherlands
E-mail: a.cordaro@amolf.nl; s.tabernig@amolf.nl; a.polman@amolf.nl

A. Cordaro
Van der Waals-Zeeman Institute
Institute of Physics
University of Amsterdam
Science Park 904, 1098 XH Amsterdam, The Netherlands

S. W. Tabernig, M. Pollard, C. Yi, B. Hoex
School of Photovoltaic and Renewable Energy Engineering
University of New South Wales
2052 Sydney, Australia

The ORCID identification number(s) for the author(s) of this article can be found under https://doi.org/10.1002/pssa.202200827.

DOI: 10.1002/pssa.202200827

 © 2023 Wiley-VCH GmbH

18626319, 0, Downloaded from https://onlinelibrary.wiley.com/doi/10.1002/pssa.202200827 by Cochrane Netherlands, Wiley Online Library on [28/02/2023]. See the Terms and Conditions (https://onlinelibrary.wiley.com/terms-and-conditions) on Wiley Online Library for rules of use; OA articles are governed by the applicable Creative Commons License

surface of a commercial interdigitated-back-contact (IBC) Si solar cell. This approach combines the advantages of Mie-resonant light scattering and Fabry–Pérot interference. We further investigate its light incoupling and trapping potential and compare it to that of standard pyramidal texturing. The geometry is placed on a flat Si cell, creating a structure that is electronically flat, minimizing surface recombination,[26] yet optically textured due to the SiN_x nanopattern. This capitalizes on the fact that SiN_x is already used as a standard layer in Si cell processing. The high refractive index of SiN_x and low optical absorption[27] over the full-relevant spectral range help create a strong resonant scattering effect.

We demonstrated our nanoscale surface incoupling geometry on a commercial interdigitated-back-contact (IBC) Si solar cell that was initially textured and for which we planarized and repassivated the front surface. We measured an enhancement of the short-circuit current density of 2.3 mA cm^{-2} compared to the flat Si surface with 75 nm SiN_x coating, reaching 36.9 mA cm^{-2} as a result of patterning the nanostructure into the SiN_x layer. The results indicate that the nanopatterned front surface is suited as an efficient light incoupling layer for thin Si solar cells.

2. Optical Optimization of the Nanopatterned SiN_x Layer

To simulate and thus optimize the optical performance of the nanopatterned SiN_x layer, we solve Maxwell's equations using Ansys Lumerical FDTD.[28] As schematically shown in the inset of **Figure 1**a, the structure consists of a square array (pitch p) of SiN_x nanodisks (height h, radius r) on a flat SiN_x residual layer (thickness t) on a Si substrate. We maximize the AM1.5G spectrum-weighted transmission into the Si absorber using a particle-swarm routine to optimize[29] the thickness of the SiN_x bottom layer, the lattice pitch, and the disks' height and diameter.

Figure 1a shows the reflectance (R) from the front surface (SiN_x and Si layers), transmittance into Si (T), and the absorptance (Abs) in SiN_x corresponding to the optimum structure with $p = 534$ nm, $h = 118$ nm, $r = 174$ nm, and $t = 59$ nm. At wavelengths shorter than 650 nm, the absorption gradually increases due to parasitic absorption in SiN_x. The AM1.5 G weighted average reflectivity is 3.5% and we observe three minima: a sharp minimum at 534 nm and two broader minima centered at 450 and 740 nm. The shape of the transmittance spectrum curve is complementary to the reflectance spectrum and is slightly reduced at shorter wavelengths due to the parasitic absorption in SiN_x.

Such high transmission can be explained by a graded-index antireflection (AR) effect combined with resonant preferential forward scattering of light. As is discussed in literature,[19,30,31] the latter can be viewed as a resonant pathway that interferes with a broader Fabry–Pérot background that can be labeled as direct pathway. On the one hand, the Fabry–Pérot background is generated by a series of four graded index layers. Indeed, the refractive index increases from that of air to that of the Si layer (n given for a wavelength of 600 nm): air ($n = 1$) is effective medium that is described by the layer of SiN_x disks in air ($n_{eff} = 1.28$),[32,33] SiN_x planar layer ($n = 1.96$)–Si ($n = 3.9$).

On the other hand, to study the resonant behavior of the nanopattern, we calculate the normalized scattering cross section (i.e., scattering cross section normalized to geometrical cross section) Q_{scat} of the single nanodisk. The broad peak in Figure 1b indicates that the disk dimensions allow for the excitation of Mie resonance inside the SiN_x pillar. Next, by inspection of the fields profiles at the wavelength of the Q_{scat} maximum $\lambda = 653$ nm, it is possible to label the resonance as a Mie-like electric dipole mode[34] (see inset of Figure 1b). This wavelength coincides with the transition from higher transmission (longer wavelengths) to lower transmission (shorter wavelengths). The forward scattering of the Mie resonance is due to the high optical mode density of the high-index Si substrate,[35,36] while the residual backward scattering can be canceled by the Fabry–Pérot background resulting in suppressed reflectance.[19]

Finally, the sharp feature in transmission at 534 nm marks the onset of diffraction in air for shorter wavelengths.[37] The transmission peak around 450 nm is close to the Fabry–Pérot resonant wavelength for a 59 nm SiN_x coating.

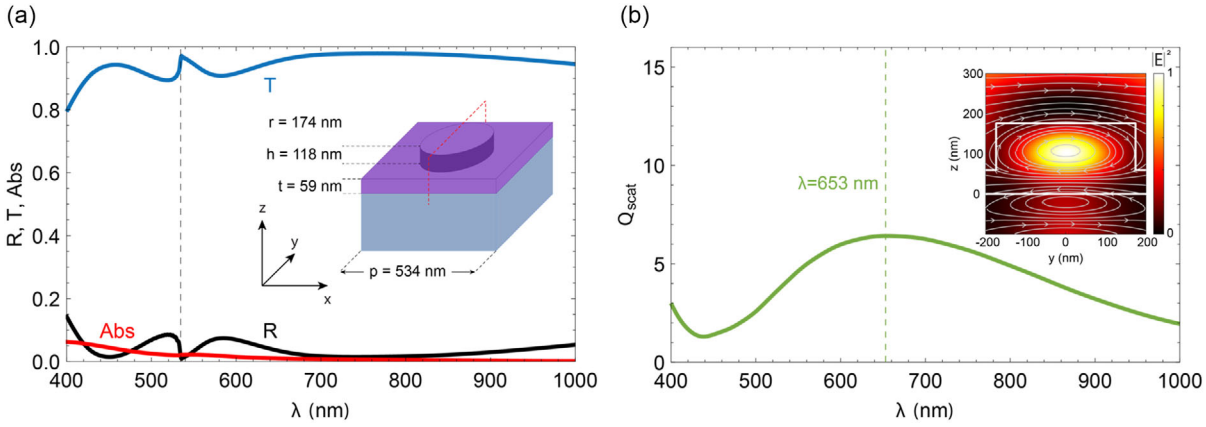

Figure 1. a) Transmittance (blue), reflectance (black), and absorptance (red) as a function of wavelength. The dashed black line indicates the onset of diffraction in air. Inset: structure (SiN_x purple, Si light blue) and dimensions for which the curves are simulated. b) Q_{scat} of the single nanodisk with dimensions reported in panel (a). Inset: crosscut through a single SiN_x disk (red dashed line in the inset of panel (a) showing a snapshot of the normalized E-field intensity and magnetic field lines (gray) for a normal-incident plane wave (total-field scattered-field source: TFSF) polarized along x at $\lambda = 653$ nm. The SiN_x interfaces are marked with solid white lines.

© 2023 Wiley-VCH GmbH

18626319, 0, Downloaded from https://onlinelibrary.wiley.com/doi/10.1002/pssa.202200827 by Cochrane Netherlands, Wiley Online Library on [28/02/2023]. See the Terms and Conditions (https://onlinelibrary.wiley.com/terms-and-conditions) on Wiley Online Library for rules of use; OA articles are governed by the applicable Creative Commons License

3. Experimental Realization on Commercial IBC Solar Cells

To apply the concept of an electronically flat optically textured SiN_x AR coating to a real device, we chose to pattern commercial interdigitated-back-contact (IBC) Si solar cells (efficiency $\eta = 21.5\%$). As acquired, these cells had a random pyramidal texture with a SiN_x AR coating on both sides and alternating n- and p-contact patches on the back. To make the cells suitable for our experiments, we removed the front texture, while the rest of the solar cell remained unprocessed. First, the textured backside was protected with a 12 µm layer of parylene-C,[38] a polymer that is resistant to a wide range of chemicals and solutions.[38] Next, the SiN_x layer was removed by HF etching until the surface appeared gray and was hydrophobic. To remove the texturing, the cell was transferred into an HNA solution (hydrofluoric acid, nitric acid, and acetic acid) that etches Si isotropically. For the case of pyramidal texture, this implies that the pyramids gradually become more round upon etching until they vanish, depending on the etch duration. This procedure allows etching solar cells down to very thin flexible foils. The etching was stopped as soon as the reflection from the Si surface appeared specular.

Figure 2a shows the sample roughness before and after the HF and HNA processing steps. The root-mean-square (RMS) roughness drops by a factor 4. Figure 2b shows the derivative of the line scans in Figure 2a; a much bigger contrast is observed between the textured and etched surfaces. This means the chemical planarization eliminated short-range roughness more strongly than long-range roughness. This made the surface well suited for the subsequent imprint process shown below. Visually, this translates into a specularly reflecting sample (Figure 2c).

The processing steps discussed so far leave the solar cell with a planar front surface but without passivating layers. This, in turn, has a severe impact on the cell performance ($\eta = 1\%$), as demonstrated by the measured 1-sun current density–voltage (J–V) characteristics in Figure 2d. In fact, removing the AR coating and pyramidal texture reduced the short-circuit current density (J_{sc}) as bare Si reflection amounts to 30–40%. However, a much stronger reduction in short-circuit current is observed in Figure 2d (black and red curves), which we ascribed to the strongly increased surface recombination at the front surface due to the absence of surface passivation.[39] Figure 2d shows how passivating the etched front surface with Al_2O_3 (10 nm, deposited by atomic layer deposition [ALD], pink curve),[40–42] followed by deposition of SiN_x (200 nm, by plasma-enhanced chemical vapor deposition [PECVD], purple curve), led to a much improved short-circuit current density and open-circuit voltage (V_{oc}). Overall, the planarization and passivation of the front surface yielded solar cells that form an effective platform for demonstrating front surface light management concepts.

Next, the optimized designed is patterned into the deposited SiN_x layer by a combination of substrate conformal imprint lithography (SCIL)[43,44] and reactive ion etching (RIE). **Figure 3**a shows an overview of the processing steps involved in the SiN_x patterning process.

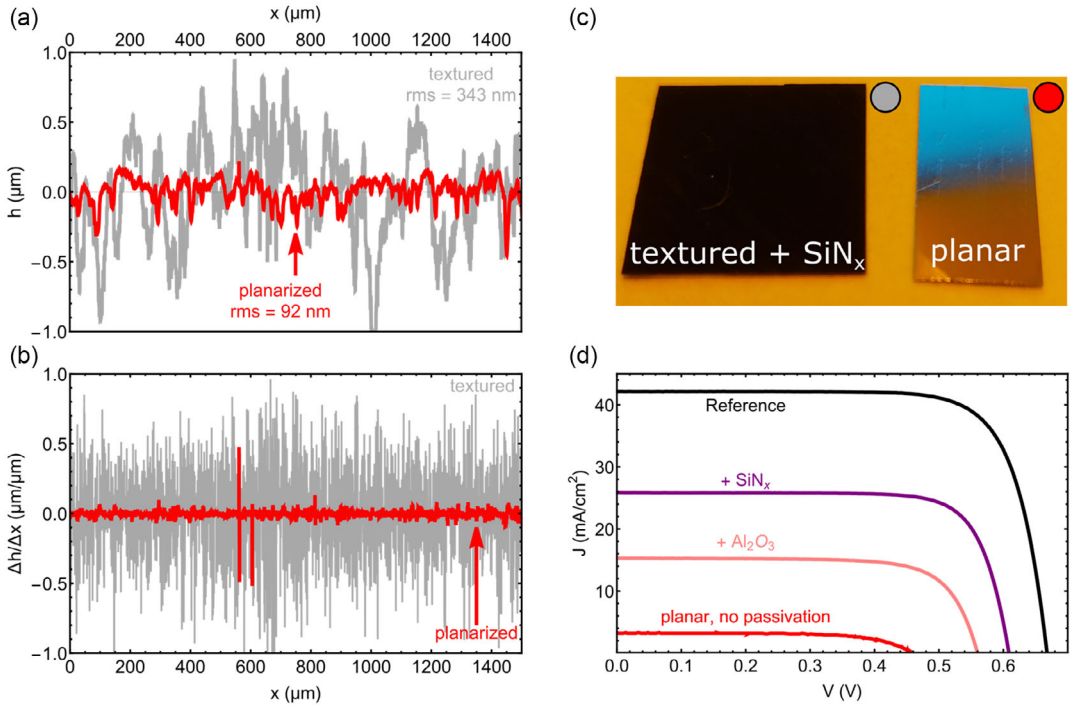

Figure 2. a) Height profiles of textured (gray) and planarized (red) Si solar cells. b) Slope profiles (change in height over distance at 100 nm intervals) for the same datasets. c) Photographs of the measured samples with standard pyramidal texture with SiN_x AR coating (left) and planarized surface without SiN_x coating (right). d) Measured current density–voltage (J–V) curves for all processing stages: textured IBC Si solar cell before processing (reference, black), after HF and HNA etching to create a planar front surface (red), after Al_2O_3 deposition (pink), and after SiN_x deposition (purple). Except for the reference J–V curve (textured), all J–V curves correspond to planar solar cells.

© 2023 Wiley-VCH GmbH

18626319, 0, Downloaded from https://onlinelibrary.wiley.com/doi/10.1002/pssa.202200827 by Cochrane Netherlands, Wiley Online Library on [28/02/2023]. See the Terms and Conditions (https://onlinelibrary.wiley.com/terms-and-conditions) on Wiley Online Library for rules of use; OA articles are governed by the applicable Creative Commons License

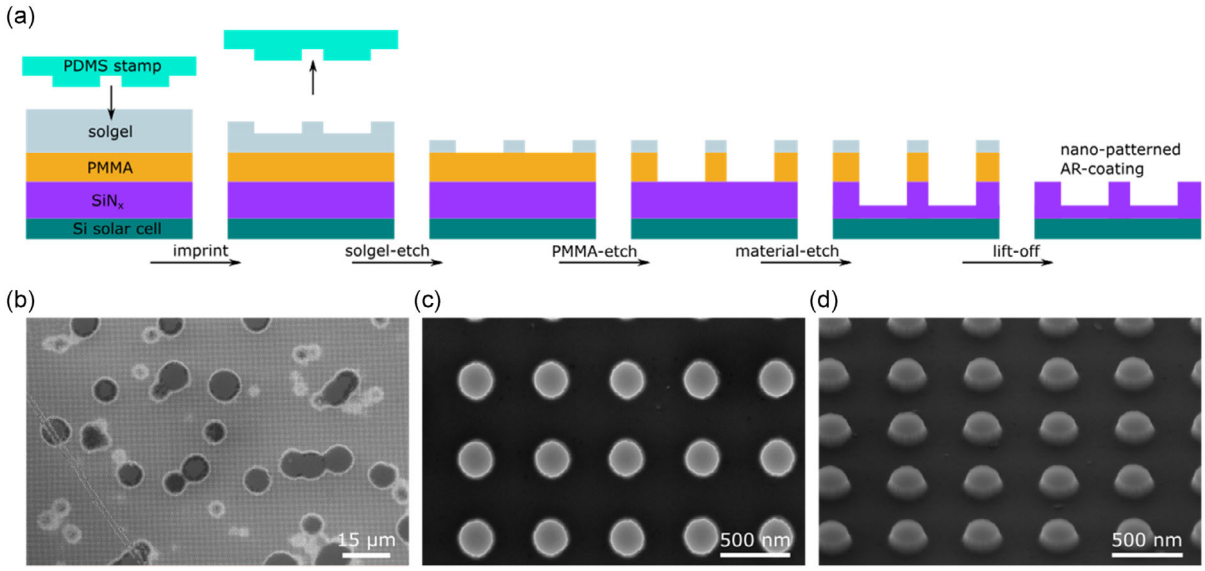

Figure 3. a) Patterning sequence. The PDMS stamp is pushed into the liquid sol–gel. After the sol–gel cured, the stamp is removed. The residual silica sol–gel layer in between the nanodisks is cleared by RIE, followed by further etching of the PMMA layer. Next, the disks are carved into SiN_x by etching further. The etch mask (silica sol–gel and PMMA) is removed by a lift-off in acetone. b) Large-scale SEM image of a patterned solar cell. Darker circular regions correspond to areas where a too thick sol–gel layer was deposited, preventing breakthrough and patterning of the SiN_x layer. c) SEM top-view image of the SiN_x disks, which appear as circles. d) Tilted SEM image of the patterned SiN_x layer, showing the cylindrical shape.

First, a PMMA layer was spin coated on the top SiN_x layer followed by a thin layer of silica sol–gel. A polydimethylsiloxane (PDMS) stamp was pressed onto the sol–gel layer while it was still liquid. The PDMS stamp was molded from a Si master-wafer nanostructured with the optimized pattern and can be reused multiple times. After 6 min of curing, in which the solvent dries to form a solid silica glass layer, the stamp was peeled off and the silica layer consisted of the desired mask pattern. Subsequently, three different RIE steps etched through the thinner sol–gel layer between the nanodisks, then through the PMMA layer, and finally into SiN_x for a duration that was controlled to obtain the desired SiN_x nanodisk height. Finally, the etch mask (PMMA and sol–gel) was lifted off in acetone, thus concluding with solar cell processing.

Figures 3b–d shows scanning electron microscope (SEM) images of the resulting nanopatterned AR coating. It is easy to notice that several sections of the surface were not well patterned. The coverage of the successfully imprinted area was determined to be around 91% in better imprinted sample regions and around 78% in sample regions with relatively many imprint defects. This is likely due to some residual long-range textures (Figure 2a), which could lead to the accumulation of excess sol–gel in pockets on the Si surface. While these regions can still be imprinted with the PDMS stamp, the resulting sol–gel layer remains thicker than in other regions. This, in turn, prevents the corresponding RIE step to break through the sol–gel layer; hence, this hinders transferring the pattern into the SiN_x. It is worth stressing that in these areas, light is still coupled into the cell, but at a lower efficiency than in the nanopatterned areas. Figure 3c,d shows high-resolution images of the patterned SiN_x disks that are uniform in size across a large area. We further note that when applied to fully planar surfaces, SCIL is well known to create fully homogenous nanopatterns without defects.[44]

4. Electronic Performance

To evaluate the effect of the nanopatterned SiN_x AR coating on the electronic performance, the J–V curves and external quantum efficiency (EQE) spectra of the solar cells were measured before and after patterning a 200 nm-thick SiN_x top layer.

Figure 4 shows the comparison for a batch of five solar cells that went through the same patterning process. For all cells, a strong gain in J_{sc} is achieved. The batch statistics in Figure 4b confirm that nanopatterning led to a systematic gain in J_{sc} of 8.5 mA cm^{-2} on average, along with a slight average V_{oc} gain, and an average fill factor (FF) reduction, dominated by a single-outlier J–V curve. Nanopatterning the SiN_x layer increased the efficiency (η) by 3.2% absolute on average compared to the 200 nm SiN_x layer flat cell, mainly due to the improved J_{sc}. The best nanopatterned cell had $J_{sc} = 36.9$ mA cm^{-2}, $V_{oc} = 0.602$ V, FF = 73.6%, and $\eta = 16.3\%$. The parameters for the initial textured, unetched cell (reference in Figure 2d) were $J_{sc} = 42.2$ mA cm^{-2}, $V_{oc} = 0.668$ V, FF = 76.2%, and $\eta = 21.5\%$. It is worth highlighting that the patterned cells showed a larger variation in J_{sc} than the planar cells (Figure 4a). We attribute this to variations in the SCIL process that did not always lead to a full imprint of the surface area (Figure 3a). Similarly, the shunting in the outlier I–V curve in Figure 4a is ascribed to unwanted effects of the SCIL process, such as damage caused by wafer handling. Nonetheless, these mentioned issues can be avoided using a fully automated SCIL imprint process, for which commercial systems are now on the market.[43]

© 2023 Wiley-VCH GmbH

18626319, 0, Downloaded from https://onlinelibrary.wiley.com/doi/10.1002/pssa.202200827 by Cochrane Netherlands, Wiley Online Library on [28/02/2023]. See the Terms and Conditions (https://onlinelibrary.wiley.com/terms-and-conditions) on Wiley Online Library for rules of use; OA articles are governed by the applicable Creative Commons License

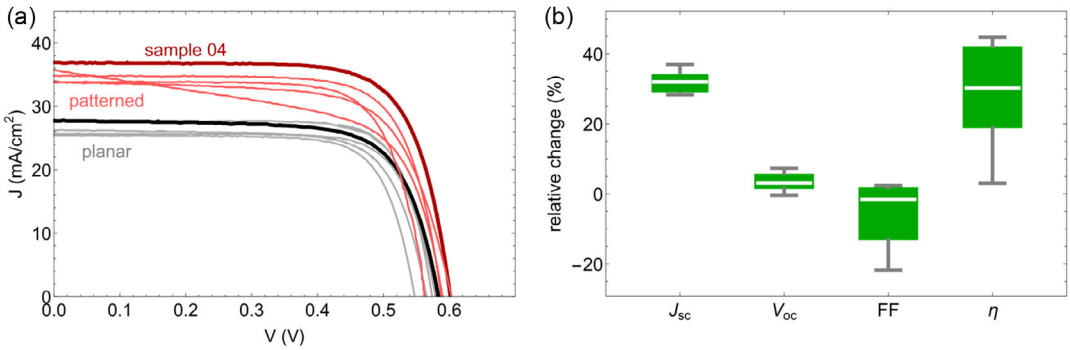

Figure 4. a) Current density–voltage (J–V) curves of planarized and passivated solar cells before (grey) and after (red) patterning of the 200 nm-thick SiN_x layer. The curves that correspond to the best cell are indicated by darker colors. b) Boxplot diagram showing the short-circuit current density (J_{sc}), open-circuit voltage (V_{oc}), FF, and efficiency for different similarly processed patterned cells (η) relative to the values for the same cells before patterning.

The large gain in J_{sc} between the patterned and flat SiN_x-coated solar cells (9.2 mA cm^{-2} for the best cell) is consistent with the strongly enhanced incoupling of light into the solar cell. To study this in detail, **Figure 5** shows the EQE of the best solar cell shown in Figure 4. Limits for the EQE, derived from the theoretical reflectivity from the cell surface, are also shown. These assume that all the light that is not reflected contributes to the EQE, even below the bandgap (dashed lines). Before patterning, the 200 nm-thick SiN_x layer resulted in an EQE spectral shape (black curve) with three peaks, and only a small spectral range (490–620 nm) showed an EQE above 80%. The calculated limit for the EQE of a Si solar cell with a planar front surface and a 200 nm SiN_x layer on top matches the experimental planar cell well for the 350 and 900 nm wavelength range. For reference, Figure 5 also shows the measured EQE and the limit for a planar cell with a 75 nm SiN_x layer, for which both curves peak at 600 nm. The cell with the 75 nm SiN_x layer received the same processing as the 200 nm SiN_x cell and showed a slightly larger gap between the theoretical curve and the measured EQE but an otherwise good agreement between 400 and 900 nm.

The measured EQE for the patterned cell shows significant improvement compared to the measured planar cells featuring both 200 and 75 nm SiN_x flat layers. In the 420–930 nm spectral range, the measured EQE for the patterned cell is above 80%. The spectral shape resembles the overall trend for the minimized reflection in the simulations in Figure 1a, shifting to a slightly lower overall current. The slight dip in the measured EQE between 450 and 600 nm is in the same range as the (larger) simulated transmission dip (Figure 1a), and the sharp feature at 534 nm observed in simulations is not visible in the experiment. We assign these differences to small variations in the nanofabrication across the cell surface.

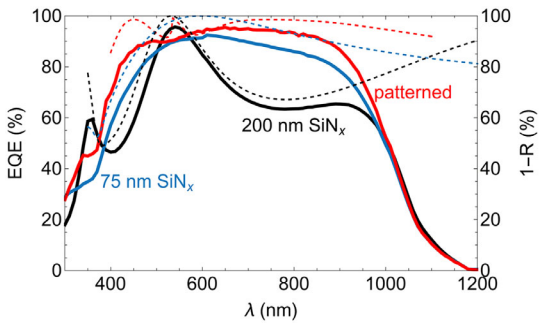

Figure 5. Measured EQE of the best cell from Figure 4. The EQE is shown for the sample before (200 nm SiN_x, black) and after (patterned, red) patterning and for a cell with single-layer AR coating (75 nm SiN_x, blue). Simulated reflection losses are shown for an air–SiN_x (200 nm)–Si stack (dashed, black), for an air–SiN_x (75 nm)–Si stack (dashed, blue), and for the optimized pattern (dashed, red).

For the present experimental cells, integrating the EQE spectrum leads to a short-circuit current that is 2.3 mA cm^{-2} above that for the planar cell with a 75 nm SiN_x AR coating. Compared to a front surface with a pyramidal texture (reference cell from Figure 2d), the SiN_x patterned device loses only 2.4 mA cm^{-2} in the 300–900 nm range (from which the maximum current that can be harvested is 33.7 mA cm^{-2}). In the near-infrared spectral range between 900 and 1200 nm (12.7 mA cm^{-2} available), the nanopatterned cells harvested 4.2 mA cm^{-2} less, which is due to nonoptimized light trapping in this spectral range. Note that the overall J_{sc} difference (6.6 mA cm^{-2}) measured during EQE measurements was larger than determined from the J–V measurements (5.3 mA cm^{-2}). This might be related to a light bias dependence of the EQE or uncertainties associated with the illumination intensity and spectrum of the light sources.

5. Conclusion

We fabricated SiN_x nanodisks arranged in a periodic lattice as an electronically flat and optically patterned AR coating on commercial IBC Si solar cells. The layer of nanodisks formed an effective AR coating embedded with Mie resonators that efficiently scatter light in a broad spectral band. The nanopatterned solar cells showed significant current gains after patterning, compared to cells with a planar surface, with the best cell achieving a J_{sc} of 36.9 mA cm^{-2} (up from 27.7 mA cm^{-2} for planar cells with 200 nm SiN_x) and a PCE of 16.3%. The measured EQE showed good agreement with the simulated transmission and reflection data, validating the combined effect of Fabry–Pérot and Mie resonances leading to enhanced light incoupling. The SCIL nanopatterning technique was found to be well suited for large-area cell processing, with some surface inhomogeneities

© 2023 Wiley-VCH GmbH

18626319, 0, Downloaded from https://onlinelibrary.wiley.com/doi/10.1002/pssa.202200827 by Cochrane Netherlands, Wiley Online Library on [28/02/2023]. See the Terms and Conditions (https://onlinelibrary.wiley.com/terms-and-conditions) on Wiley Online Library for rules of use; OA articles are governed by the applicable Creative Commons License

that can be avoided using an automated imprint system and better planarization. Using the planar nanopatterned geometry instead of conventional macroscopic surface texture led to a short-circuit current deficit of about 4.2 mA cm^{-2} due to reduced light trapping in the 900–1200 nm spectral band. Overall, the results shown provide a roadmap for the development of wafer-based flexible solar cells, where the nanopatterned SiN_x can replace the conventional macroscopic surface texture for efficient light incoupling in silicon solar cells that are just a few micrometers thick.

6. Experimental Section

Dependence of Electronic Parameters on Annealing Treatment for Improved Passivation: Annealing (400 °C, 10 min, ambient) of the solar cell to improve the Al_2O_3 passivation[45] usually does not affect the solar cell negatively. In some cases, we have found that it affected the FF negatively. **Figure 6** shows a comparison between two batches (11–12 samples each) that were fabricated identically during the same fabrication run, with the only difference being that one was annealed after Al_2O_3 and SiN_x deposition, and the other was not.

It becomes clear that annealing improves the J_{sc} and EQE significantly (2 mA cm^{-2} on average). At the same time, the V_{oc} also strongly increases (60 mV on average), but these gains are offset by a large loss in FF (from 75% down to 40%). This large drop in FF does not always occur, but to ensure that the solar cell devices remain comparable to one another, we chose to work with the not-annealed batch for fabrication. We believe that this significant drop in FF was related to proprietary features of the commercial IBC solar cells used in this work. Consequently, as we expected annealing to cause and overall loss in efficiency, we worked with the unannealed samples.

Measured Reflection: **Figure 7** shows the measured specular reflectance of the best cell (i.e., "sample 04" in Figure 4 and "patterned" from Figure 5) and its finite-difference time-domain (FDTD)-simulated counterpart corresponding to the ideal optimized pattern. For comparison, the calculated reflection of a 75 nm-thick SiN_x layer on Si is also shown. The differences between simulated and measured spectra could be attributed to fabrication imperfections.

Optical Simulations: For Figure 1, Ansys Lumerical FDTD[28] was used to solve Maxwell's equations numerically. The simulation mesh accuracy was determined by mesh convergence testing. Periodic boundary conditions were used to reproduce the unit cell in both directions along the Si surface plane. Perpendicular to the plane, perfectly matched layers (PML) were used at the boundaries. A broadband plane wave source was used, and the monitor used to detect the transmission was inserted at the

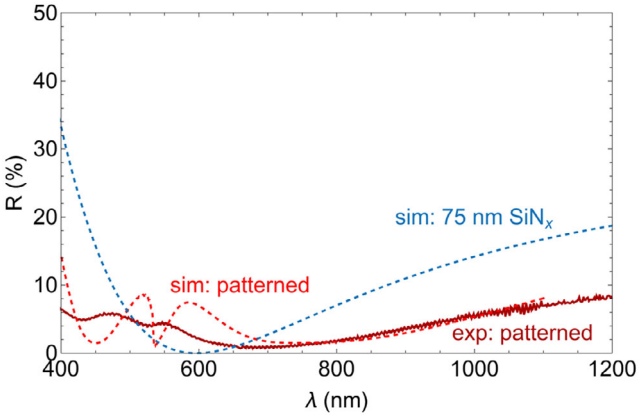

Figure 7. Measured (solid dark red line) and simulated (dashed red line) specular reflectance of the best cell shown in Figure 4 under unpolarized normal incident illumination. The blue dashed line indicates the calculated reflection of a 75 nm-thick SiN_x layer on Si.

SiN_x–Si interface. The simulation was conducted for various structure parameters, which were adapted according to a particle swarm optimization. The scattering cross section and field profile was obtained from single-particle scattering simulation, which used PMLs at all simulation boundaries, and a TFSF source.

Planarization: To planarize the front side of the double-textured solar cells, their backside was protected using the parylene-C polymer. It was deposited by vaporizing a solid parylene dimer precursor and by splitting it into monomers at high temperature (650 °C). The hot vapor was channeled into a cool (room temperature) chamber that contained the cells, where the vapor formed the polymer on all exposed surfaces. Parylene-C was resistant to all chemicals used for processing. For electronic characterization, the parylene layer that covered the contacts was removed with a RIE (O_2 at 20 sccm, 200 W, 15 mTorr, 90–150 min). The initial SiN_x layer on the solar cell was removed by dipping the parylene-protected solar cell into HF solution (4.5%, ≈10 min, no agitation) until the front surface appeared gray and hydrophobic. The planarization was done by HNA etching. Great care for personal safety must be taken during this process, as the used chemicals are extremely hazardous in their individual and combined form. Hydrofluoric acid (HF, 49%), nitric acid (HNO_3, 70%), and acetic acid (CH_3COOH, glacial) were mixed at a ratio 10:73:17, according to Yu et al.[46] A stirring bar is added to 500 mL of HNA solution and accelerated the etch rate (typically by a factor 4). The parylene-protected solar cell was dipped in the solution, and the planarization was monitored by

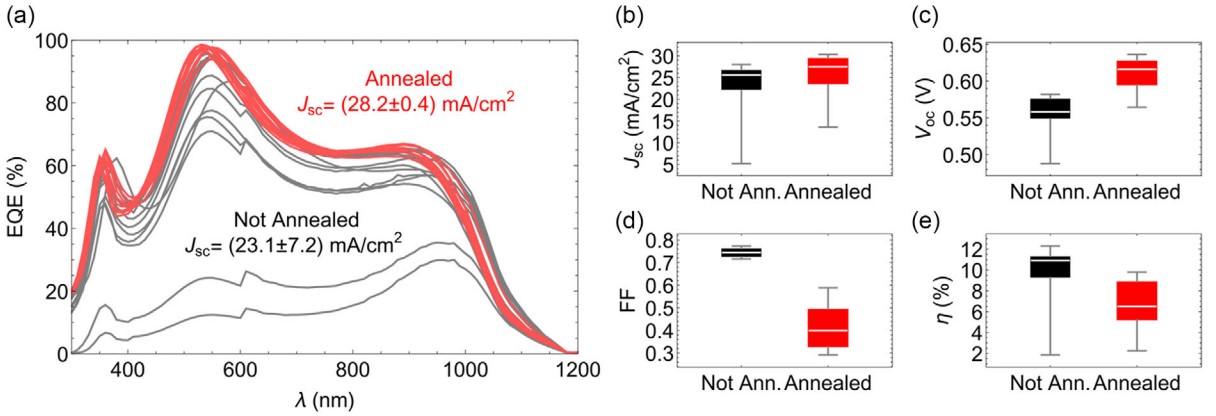

Figure 6. a) EQE of cells of two distinct batches. One batch of samples was annealed (red) and the other batch not (gray). b–e) Short-circuit current density (J_{sc}), open-circuit voltage (V_{oc}), FF, and efficiency (η) for the annealed (red) and not-annealed (black) batch.

© 2023 Wiley-VCH GmbH

18626319, 0, Downloaded from https://onlinelibrary.wiley.com/doi/10.1002/pssa.202200827 by Cochrane Netherlands, Wiley Online Library on [28/02/2023]. See the Terms and Conditions (https://onlinelibrary.wiley.com/terms-and-conditions) on Wiley Online Library for rules of use; OA articles are governed by the applicable Creative Commons License

looking at the gradually increasing specularity of the initially diffused Si surface. Depending on the agitation and the HNA volume, planarization took 15–60 min. Afterward, the samples were taken out of the solution and thoroughly rinsed in water.

Patterning: We used substrate conformal soft-imprint lithography (SCIL)[43,44] for the patterning. Silica sol–gel was spin coated at 2000 RPM for 8 s, to form a layer of 74 nm thickness. The stamp was pushed into the liquid silica gel and removed after 6 min of curing at room temperature. The stamp dimensions are the same as in Figure 1, except for the height of the pillars. The height of the pillars and the thickness of the bottom layer were regulated with the initial SiN_x thickness and the etch duration. To etch specific layers, we used the following RIE chemicals, of which the durations were adjusted depending on the desired thickness: silica sol–gel was etched with CHF_3/Ar. PMMA was etched by O_2. SiN_x was etched by CHF_3/O_2.

Passivation: For the passivation of the planar front surface with Al_2O_3, the solar cell surface was cleaned with an RCA cleaning procedure.[47] Sequentially, the sample was dipped in RCA-1 ($H2O_2$:NH_4OH:H_2O (1:1:5); 80 °C; 10 min), RCA-2 (H_2O_2:HCl:H_2O (1:1:5); 80 °C; 10 min), and HF (4.5%, 2 min). The sample was blow dried with a N_2 gun after the HF cleaning step. Within 30 min after the last cleaning step, the sample was loaded and under vacuum in a Picosun R-200 ALD system. The cell was heated to 200 °C, and 100 cycles of a water (H_2O) and tetramethylaluminum (TMA) deposition sequence were run to deposit 10 nm of Al_2O_3. The SiN_x layer was deposited by PECVD, using an Oxford Instruments Plasmalab 100 PECVD tool. The SiN_x layer (180-200 nm) was deposited at 300 °C from silane (SiH_4) and ammonia (NH_3) precursors. To improve the Al_2O_3 passivation, an annealing step was done in some cases. The cells were deposited on a 400 °C hot Si wafer on a hotplate and left there for 10 min in air.

Optical Characterization: Specular reflectance (normal incidence) was measured using a Filmetrics F20 tool. The sampled area corresponded to a disk of around 1 mm-diameter. The reflectance data was collected for the range between 200 and 1728 nm.

Electronic Characterization: For the electronic characterization, the solar cells were mounted on a stage with an aperture ($8 \times 8\ mm^2$) that was smaller than the solar cell area ($20 \times 10\ mm^2$). The cell was contacted from the back, with two (EQE) or four (*I*–*V*) contacting probes pressing the cell onto the aperture rim, thereby fixing its position. The stage was then flipped over so that the front surface of the solar cell faced upward in the AM1.5 solar simulator. For the EQE measurements, PV measurements QEX7 system were used. The samples were brought into a focal spot with dimensions $1 \times 4\ mm^2$ under bias light. Current–voltage (*I*–*V*) curves were measured using a WaveLabs SINUS 220 tool. The obtained current values were normalized by the aperture size ($8 \times 8\ mm^2$ in most cases) to obtain the current density.

Acknowledgements

This work is part of the research programme of the Dutch Research Council (NWO).

Conflict of Interest

The authors declare no conflict of interest.

Author Contributions

A.C. and S.W.T. contributed equally to the work. A.C. performed optical simulations. S.W.T., M.P., and C.Y.: fabricated and characterized the interdigitated-back-contact cells. S.W.T. and A.C. performed fabrication of the nanostructured coating. S.W.T., A.C., and M.P.: characterized the patterned solar cells. B.H., E.A.L., M.P., and A.P.: supervised the project. All authors contributed to the writing of the manuscript and gave feedback.

Data Availability Statement

The data that support the findings of this study are available from the corresponding author upon reasonable request.

Keywords

antireflection, Mie scattering, nanostructure, silicon solar cell, thin-film Si

Received: November 30, 2022
Revised: January 5, 2023
Published online:

[1] A. Groenewolt, J. Bakker, J. Hofer, Z. Nagy, A. Schlüter, *Int. J. Energy Environ. Eng.* **2016**, *7*, 261.
[2] Solarge, Solarge (website), n.d.
[3] Y. Ota, T. Masuda, K. Araki, M. Yamaguchi, *Coatings* **2018**, *8*, 432.
[4] T. Tayagaki, K. Araki, M. Yamaguchi, T. Sugaya, *IEEE J. Photovoltaics* **2019**, *9*, 1721.
[5] Lightyear, n.d.
[6] M. Hatamvand, E. Kamrani, M. Lira-Cantú, M. Madsen, B. R. Patil, P. Vivo, M. S. Mehmood, A. Numan, I. Ahmed, Y. Zhan, *Nano Energy* **2020**, *71*, 104609.
[7] S. Wang, B. D. Weil, Y. Li, K. X. Wang, E. Garnett, S. Fan, Y. Cui, *Nano Lett.* **2013**, *13*, 4393.
[8] R. Saive, *Prog. Photovoltaics Res. Appl.* **2021**, *29*, 1125.
[9] J. Trube, S. Herritsch, International Technology Roadmap for Photovoltaic (ITRPV), **2022**.
[10] A. Augusto, J. Karas, P. Balaji, S. G. Bowden, R. R. King, *J. Mater. Chem. A* **2020**, *8*, 16599.
[11] V. Alex, S. Finkbeiner, J. Weber, *J. Appl. Phys.* **1996**, *79*, 6943.
[12] M. C. Raval, S. M. Reddy, in *Solar Cells*, IntechOpen, London, **2019**, https://doi.org/10.5772/intechopen.84817.
[13] T. E. Scheul, E. Khorani, T. Rahman, M. D. B. Charlton, S. A. Boden, *Prog. Photovoltaics Res. Appl.* **2020**, *28*, 1248.
[14] A. Alasfour, Z. J. Yu, W. Weigand, D. Quispe, Z. C. Holman, *Sol. Energy Mater. Sol. Cells* **2020**, *218*, 110761.
[15] S. Zhong, W. Wang, M. Tan, Y. Zhuang, W. Shen, *Adv. Sci.* **2017**, *4*, 1700200.
[16] Y. Li, H. Sai, T. Matsui, Z. Xu, V. H. Nguyen, Y. Kurokawa, N. Usami, *Sol. RRL* **2022**, *6*, 2200707.
[17] H. Savin, P. Repo, G. Von Gastrow, P. Ortega, E. Calle, M. Garín, R. Alcubilla, *Nat. Nanotechnol.* **2015**, *10*, 624.
[18] T. H. Fung, T. Veeken, D. Payne, B. Veettil, A. Polman, M. Abbott, *Opt. Express* **2019**, *27*, 38645.
[19] A. Cordaro, J. van de Groep, S. Raza, E. F. Pecora, F. Priolo, M. L. Brongersma, *ACS Photonics* **2019**, *6*, 453.
[20] U. Sikder, M. A. Zaman, *Opt. Laser Technol.* **2016**, *79*, 88.
[21] N. Tavakoli, R. Spalding, A. Lambertz, P. Koppejan, G. Gkantzounis, C. Wan, R. Röhrich, E. Kontoleta, A. F. Koenderink, R. Sapienza, M. Florescu, E. Alarcon-Llado, *ACS Photonics* **2022**, *9*, 1206.
[22] E. Camarillo Abad, H. J. Joyce, L. C. Hirst, *ACS Photonics* **2022**, *9*, 2724.
[23] P. M. Piechulla, L. Muehlenbein, R. B. Wehrspohn, S. Nanz, A. Abass, C. Rockstuhl, A. Sprafke, *Adv. Opt. Mater.* **2018**, *6*, 1701272.
[24] P. M. Piechulla, E. Slivina, D. Bätzner, I. Fernandez-Corbaton, P. Dhawan, R. B. Wehrspohn, A. N. Sprafke, C. Rockstuhl, *ACS Photonics* **2021**, *8*, 3476.
[25] P. M. Piechulla, B. Fuhrmann, E. Slivina, C. Rockstuhl, R. B. Wehrspohn, A. N. Sprafke, *Adv. Opt. Mater.* **2021**, *9*, 2100186.
[26] A. G. Aberle, *Sol. Energy Mater. Sol. Cells* **2001**, *65*, 239.

© 2023 Wiley-VCH GmbH

18626319, 0, Downloaded from https://onlinelibrary.wiley.com/doi/10.1002/pssa.202200827 by Cochrane Netherlands, Wiley Online Library on [28/02/2023]. See the Terms and Conditions (https://onlinelibrary.wiley.com/terms-and-conditions) on Wiley Online Library for rules of use; OA articles are governed by the applicable Creative Commons License

[27] K. Luke, Y. Okawachi, M. R. E. Lamont, A. L. Gaeta, M. Lipson, *Opt. Lett.* **2015**, *40*, 4823.
[28] Ansys Lumerical, n.d.
[29] J. Kennedy, R. Eberhart, in *Proc. ICNN'95 - Int. Conf. Neural Networks*, IEEE, Piscatway, NJ n.d., pp. 1942–1948.
[30] S. Fan, W. Suh, *J. Opt. Soc. Am. A* **2003**, *20*, 569.
[31] H. A. Haus, *Waves And Fields In Optoelectronics*, Prentice-Hall, Englewood Cliffs, N.J, **1984**.
[32] M. E. Motamedi, W. H. Southwell, W. J. Gunning, *Appl. Opt.* **1992**, *31*, 4371.
[33] T. K. Gaylord, W. E. Baird, M. G. Moharam, *Appl. Opt.* **1986**, *25*, 4562.
[34] J. Van De Groep, A. Polman, *Opt. Express* **2013**, *21*, 1253.
[35] T. J. Kippenberg, A. L. Tchebotareva, J. Kalkman, A. Polman, K. J. Vahala, *Phys. Rev. Lett.* **2009**, *103*, 027406.
[36] P. Spinelli, M. Verschuuren, A. Polman, *Nat. Commun.* **2012**, *3*, 692.
[37] C. Palmer, E. Loewen, *Diffraction Grating Handbook*, **2005**.
[38] M. Golda-Cepa, K. Engvall, M. Hakkarainen, A. Kotarba, *Prog. Org. Coatings* **2020**, *140*, 105493.
[39] J. Schmidt, F. Werner, B. Veith, D. Zielke, S. Steingrube, P. P. Altermatt, S. Gatz, T. Dullweber, R. Brendel, *Energy Procedia* **2012**, *15*, 30.
[40] B. Hoex, S. B. S. Heil, E. Langereis, M. C. M. Van De Banden, W. M. M. Kessels, *Appl. Phys. Lett.* **2006**, *89*, 042112.
[41] B. Hoex, J. J. H. Gielis, M. C. M. Van De Sanden, W. M. M. Kessels, *J. Appl. Phys.* **2008**, *104*, 113703.
[42] B. Hoex, J. Schmidt, P. Pohl, M. C. M. Van De Sanden, W. M. M. Kessels, *J. Appl. Phys.* **2008**, *104*, 044903.
[43] M. A. Verschuuren, M. Megens, Y. Ni, H. van Sprang, A. Polman, *Adv. Opt. Technol.* **2017**, *6*, 243.
[44] M. A. Verschuuren, M. W. Knight, M. Megens, A. Polman, *Nanotechnology* **2019**, *30*, 345301.
[45] M. Pawlik, J. P. Vilcot, M. Halbwax, D. Aureau, A. Etcheberry, A. Slaoui, T. Schutz-Kuchly, R. Cabal, in *Energy Procedia*, Elsevier Ltd., Amsterdam **2014**, pp. 85–89.
[46] Z. J. Yu, B. M. Wheelwright, S. Manzoor, Z. C. Holman, *J. Mater. Sci. Mater. Electron.* **2016**, *27*, 10270.
[47] W. Kern, *J. Electrochem. Soc.* **1990**, *137*, 1887.

© 2023 Wiley-VCH GmbH

18626319, 0, Downloaded from https://onlinelibrary.wiley.com/doi/10.1002/pssa.202200827 by Cochrane Netherlands, Wiley Online Library on [28/02/2023]. See the Terms and Conditions (https://onlinelibrary.wiley.com/terms-and-conditions) on Wiley Online Library for rules of use; OA articles are governed by the applicable Creative Commons License